All-Weather Hyperspectral Atmospheric Sounding

William J. Blackwell, R. Vincent Leslie, Michael L. Pieper, and Jenna E. Samra

Development of a new hyperspectral microwave (HM) remote sensing modality for all-weather atmospheric sounding has been enabled by recent advances in microwave device technology driven largely by the commercial communications sector. A spaceborne HM sounder would substantially improve weather forecasting by offering both cloud penetration and high vertical resolution.

» **Remote measurements of Earth's atmospheric** state using microwave and infrared wavelengths have been carried out for many years [1, 2]. Physical considerations involving the use of these spectral regions include the relatively high cloud-penetrating capability at microwave wavelengths and the relatively sharp weighting functions at infrared wavelengths, particularly in the shortwave region near 4 μm in which Planck nonlinearity further increases temperature sensitivity. Infrared spectrometer technology has advanced markedly over the last 15 years or so, leading to the simultaneous spectral sampling of thousands of bands spaced along narrow atmospheric absorption features [3]. The Atmospheric InfraRed Sounder (AIRS), launched in May 2002, measures 2378 channels from 3.7 to 15.4 μm and the Infrared Atmospheric Sounding Interferometer (IASI), launched in 2006, measures 8461 channels from 3.6 to 15.5 μm [4, 5]. These sensors, and similar sensors to be launched as part of the National Polar-orbiting Operational Environmental Satellite System (NPOESS) and Meteorological Satellite (Meteosat) Third Generation systems, substantially improve atmospheric sounding through the use of hyperspectral measurements, which yield greater vertical resolution throughout the atmosphere [6].

Global simulation studies over ocean and land in clear and cloudy atmospheres use three different atmospheric profile databases to assess the temperature, moisture, and precipitation sounding capability of several notional hyperspectral microwave systems with channels sampled near the 50–60, 118.75, and 183.31 GHz absorption lines. These analyses demonstrate that hyperspec-

tral microwave operation using frequency multiplexing techniques substantially improves temperature- and moisture-profiling accuracy, especially in atmospheres that challenge conventional non-hyperspectral microwave sounding systems because of high water vapor and cloud liquid water content. Retrieval performance studies compare hyperspectral microwave sounding performance to conventional microwave and hyperspectral infrared approaches, both in a geostationary and low Earth-orbit context, and a path forward to a new generation of high-performance all-weather sounding is discussed.

Hyperspectral Microwave Concepts

A spate of recent technology advances driven in part by the gigabit wireless communications industry, the semiconductor industry, and the NASA Earth Science Technology Office has significantly and profoundly changed the landscape of modern radiometry by enabling miniaturized, low-power, and low-noise radio-frequency receivers operating at frequencies up to 200 GHz [7–9]. These advances enable the practical use of receiver arrays to multiplex multiple broad-frequency bands into many spectral channels; the atmospheric sounding benefit of such systems is explored in this article. The term *hyperspectral microwave* refers generically to microwave sounding systems with approximately 100 spectral channels or more. In the infrared wavelength range, the term *hyperspectral* is used to denote the resolution of individual, narrow absorption features that are abundant throughout the infrared spectrum. In the microwave and millimeter wavelength range, however, there are substantially fewer spectral features and the spectral widths are typically broad, and an alternate definition is therefore appropriate.

Initial analysis started with geostationary sounding systems. Low Earth-orbiting systems are considered later in the article. Detailed studies of the geophysical products that could be derived from a geostationary microwave sensor and the radiometric requirements of such a sensor date back many years [10, 11]. The persistent observations afforded by a geostationary platform would allow temporal sampling over most of the viewable Earth hemisphere on time scales of approximately five minutes. The capability to sound in and around storms would significantly improve both regional and global numerical weather prediction models. Tropospheric information content of infrared observations, however, is compromised by clouds, which attenuate the radiance to space from the atmosphere below the cloud level. The ability to model and forecast hurricanes would greatly improve with microwave measurements from geostationary orbit.

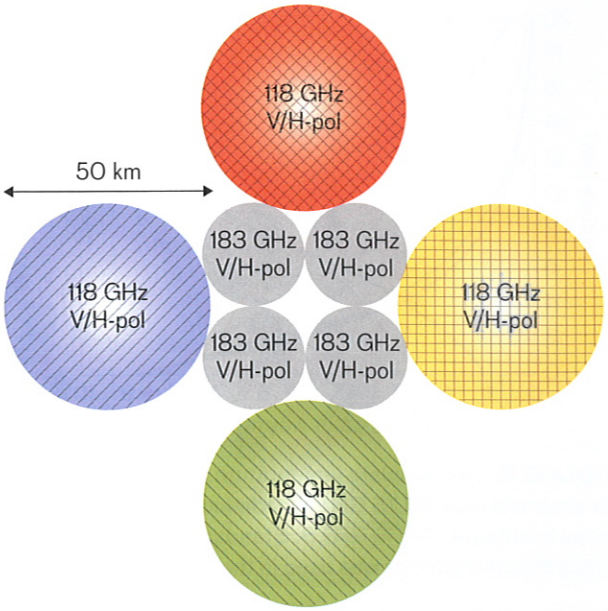

FIGURE 1. The pattern shows the instantaneous antenna beam 3 dB antenna power contours for a notional multiplexed hyperspectral millimeter-wave array spectrometer operating near 118 and 183 GHz.

A simple example of a multiplexed hyperspectral microwave system is shown in Figure 1 with eight instantaneous fields of view (IFOVs), four near 118 GHz and four near 183 GHz. Each IFOV is sampled by a single feedhorn measuring two orthogonal polarizations (vertical and horizontal, for example) that are each fed to a ten-channel spectrometer. The cross-hatching in the figure indicates slightly different frequency bands. The 183 GHz IFOVs each measure the same spectral channels. As the array is microscanned in two dimensions, each 50 km spot on the ground is eventually sampled by 80 channels near 118 GHz, and each 25 km spot on the ground is eventually sampled by 20 channels near 183 GHz for a total of one hundred channels. Additional channels could be added by increasing the number of feeds and receiver banks, and hyperspectral microwave systems with hundreds of channels are therefore reasonable. Note that further channelization within a given receiver bandwidth quickly reaches a point of diminishing returns because of the increase in thermal noise as 1/sqrt(B), where B is

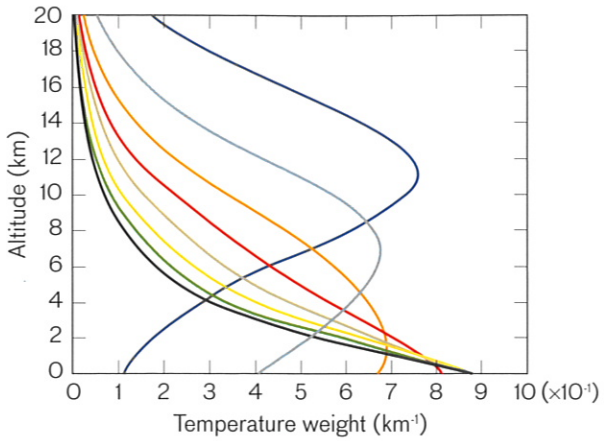

FIGURE 2. The template temperature weighting functions for channels near 118.75 GHz at nadir incidence span the range in altitude. The 1976 U.S. Standard Atmosphere over a nonreflective surface was used in the calculations.

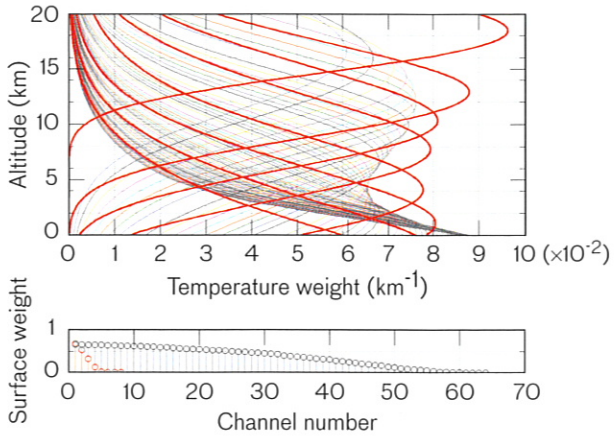

FIGURE 3. The weighting functions for 64 channels near 118.75 GHz and the eight ATMS tropospheric temperature sounding channels near 50–57 GHz at nadir incidence show a similar coverage of all altitudes as in Figure 2.

the bandwidth for a single channel. Detailed analyses by other investigators (see [12], for example) demonstrate that a division into about eight to ten channels per receiver yields near optimal results.

Another illustration of the spectral multiplexing concept uses temperature weighting functions. The temperature weighting function, given by the derivative of the transmittance function with respect to altitude, characterizes the degree to which each atmospheric layer contributes to the radiances viewed from space at the indicated frequencies. The weighting functions approach zero at high altitudes, where the atmosphere becomes transparent, or at low altitudes, where the overlying atmosphere is so thick as to be fully opaque. The temperature weighting functions at nadir incidence for a nominal eight-channel receiver operating in a 5 GHz bandwidth on the low-frequency side of the 118.75 GHz oxygen line are shown in Figure 2. The 1976 U.S. Standard Atmosphere over a nonreflective surface was used in the calculations. The channels are equally spaced in frequency, and the bandwidth of each channel is 560 MHz.

A hyperspectral microwave system can be constructed by using multiple receiver banks with a replicated, but frequency-shifted, version of the template channel set used to generate Figure 2. For example, eight receiver banks with eight channels each could be used to create a 64-channel system by progressively shifting the intermediate-frequency (IF) band of each receiver by 70 MHz.

The temperature weighting functions of the 64-channel multiplexed system can now be compared to those of a current-generation microwave sounder, the Advanced Technology Microwave Sounder (ATMS), scheduled to fly on board the NPOESS Preparatory Project in 2011 [13]. In the upper panel of Figure 3, the set of weighting functions for the 64-channel system is indicated by thin lines and the eight tropospheric ATMS channels are indicated by heavy lines. The surface weights of all channels are shown in the lower panel of Figure 3. The frequencies for the eight ATMS channels shown range from 50.3 GHz (most transparent) to 57.29 GHz. The effective atmospheric vertical sampling density of the 64-channel multiplexed system is clearly superior to the conventional 8-channel system. Water-vapor-burden weighting functions are not shown here, as similar arguments apply. The temperature and water-vapor profiling advantage resulting from fine vertical atmospheric sampling is discussed later.

The temperature weighting function for the ATMS 50.3 GHz channel is shown near the bottom of the top panel of Figure 3 (the temperature weight near the surface is ~0.06 km^{-1}), and this channel is significantly more transparent than the most transparent 118 GHz channel (the temperature weight near the surface is ~0.09 km^{-1}) because of water-vapor continuum absorption, but the weighting function has a comparable shape. Water-vapor absorption appears to be a significant handicap for millimeter-wave sounding [10]. Hyperspectral millimeter-wave systems, however, are not so adversely affected because of the very dense vertical spacing of the weighting functions in the atmospheric boundary layer (discussed in detail later in this article).

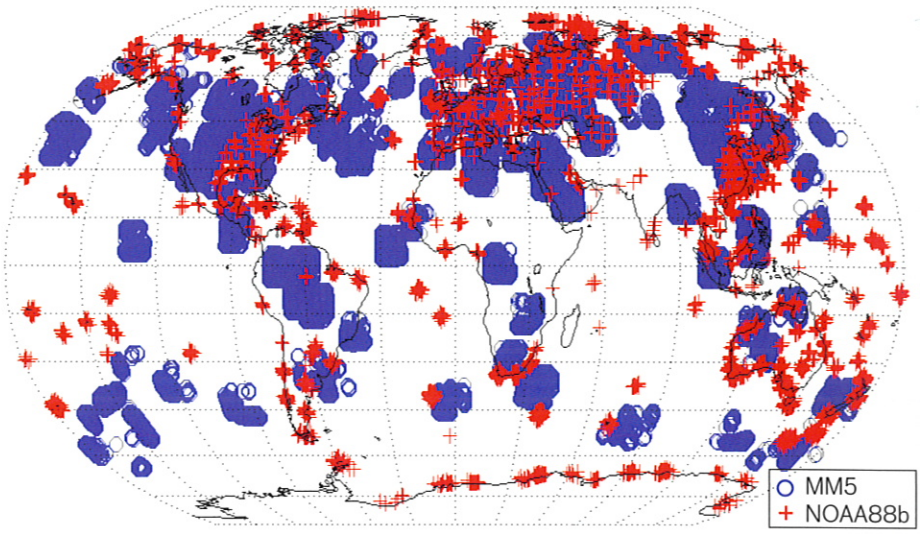

FIGURE 4. The markers indicate the geographical locations of the pixels contained in the MM5 and NOAA88b data sets. Global coverage includes a variety of land and ocean pixels.

Experimental Process

Three important concepts are introduced here: the new sensing methodology, the optimization process, and the benefits to the sensing community. First, a frequency-multiplexing technique can be used to realize hyperspectral microwave measurements with conventional receiver hardware. The approach is easily scalable and requires no new technology development. Second, the relative merits of increased bandwidth versus increased channelization within an increased bandwidth are examined, and the optimal operating point depends on the available integration time. Third, a set of comprehensive and global simulation analyses with state-of-the-art retrieval methods illuminates many of the principal dimensions of the design and performance-comparison trade space, including 60 GHz versus 118 GHz, hyperspectral microwave versus conventional microwave, and hyperspectral microwave versus hyperspectral infrared. In addition, both geostationary and low Earth-orbit configurations are considered. Note that these areas are certainly not mutually exclusive, and an optimized sounding system will likely contain several of these components.

Opacity from water-vapor continuum absorption is a fundamental limitation of conventional millimeter-wave sounding, but the proposed hyperspectral millimeter-wave approach can be used to overcome this limitation. All retrievals presented in this article are carried out using neural networks trained against cloud-resolving physical models, and the methodologies used to initialize, train, and evaluate the neural network retrievals are discussed.

A variety of notional systems compare the hyperspectral microwave approach with current and planned approaches that use microwave and hyperspectral infrared observations separately and in combination. Temperature, water-vapor, and precipitation-retrieval performance comparisons are then presented, and the impact of correlated error sources on performance is examined.

The goal of this project was to demonstrate the viability of hyperspectral microwave sounding, a new remote-sensing modality, through the use of detailed and comprehensive simulation studies. Conventional microwave sounders typically employ approximately 20 spectral channels; our method proposes the use of approximately 100 spectral channels, achieved using multiple radio-frequency receiver arrays at slightly different center frequencies that sample the same spot on the Earth. The additional channels yield improved sampling in the vertical dimension of the atmosphere.

Data Sets and Physical Models

These performance comparisons are all based on simulated observations derived using physical models and global ensembles of atmospheric states. The selection of the ensemble of atmospheric states is a critically important part of any simulation study, and great care has been taken to ensure that the profiles included in the analysis are sufficiently representative of the cloudy, moist atmospheres that challenge most atmospheric sounding systems.

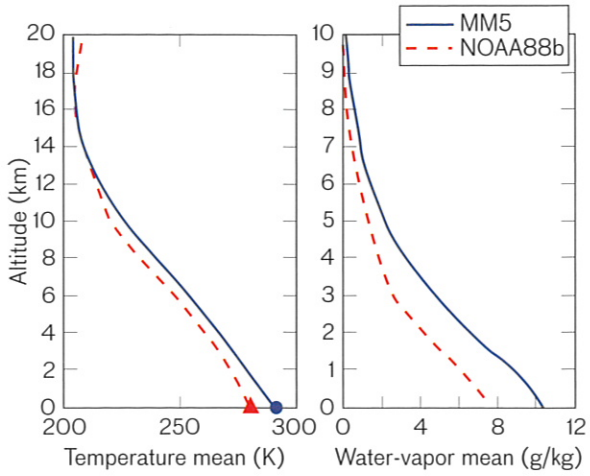

FIGURE 5. The MM5 and NOAA88b data sets show similar temperature and water-vapor profiles. However, the MM5 data are more representative of weather conditions near precipitation systems, with higher temperatures and humidity at all altitudes.

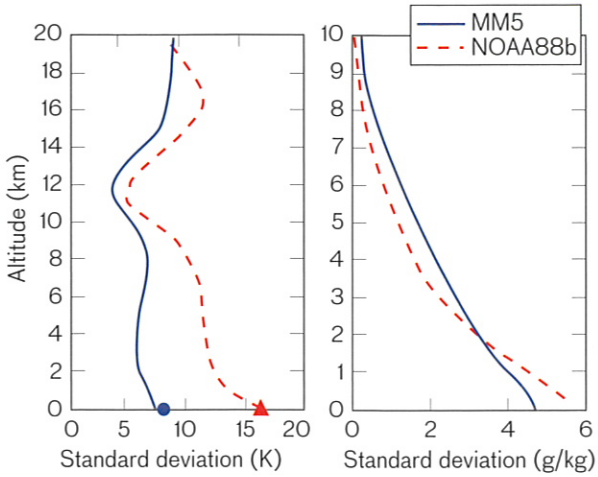

FIGURE 6. As with the mean temperature and water-vapor data in Figure 5, the standard deviations in the MM5 and NOAA88b data also show similar properties. Note, however, that the standard deviations of the NOAA88b data are greater than those of the MM5 data at low altitudes.

NOAA88b Atmospheric Profile Data Set

The National Oceanic and Atmospheric Administration NOAA88b radiosonde/rocketsonde data set contains 7547 profiles, globally distributed seasonally and geographically, as shown in Figure 4. Atmospheric temperature, moisture, and ozone are given at 100 discrete levels from the surface to altitudes exceeding 50 km. Skin surface temperature is also recorded. NOAA88b water-vapor measurements above approximately 10 km are of questionable quality and are not considered in this article. Approximately 6500 profiles from the NOAA88b database were selected for inclusion in this study by eliminating cases for which the surface pressure was not equal to 1000 mbar. The mean and standard deviation of the temperature and water-vapor profiles in the NOAA88b data set are shown in Figure 5 and Figure 6, respectively.

MIT MM5 Precipitation and Atmospheric Profile Data Set

The MIT MM5 precipitation and atmospheric profile data set is composed of meteorological parameters for 122 storms simulated using the fifth-generation NCAR/Penn State Mesoscale Model (MM5) [14, 15]. These storms are globally distributed as illustrated in Figure 4 and span a year. Each storm has 190 × 190 picture elements (pixels) spaced on a rectangular 5 km grid with 42 pressure levels. About 46% of the 4.4 million pixels are precipitating with nonzero rain water or snow at 1000 mbar [14]. This percentage of precipitating pixels is high because only stormy regions were sampled. The validity of this ensemble of storms has been shown by the statistical agreement between its simulated brightness temperatures and those coincidentally observed by the Advanced Microwave Sounding Unit (AMSU) instruments aboard NOAA-15, -16, and -17 satellites [14, 15].

Approximately 50,000 nonprecipitating pixels selected from the 122 storm cases were used in this study; approximately half of these pixels were cloudy (nonzero integrated cloud liquid-water content). Precipitation was screened by requiring that the sum of vertically averaged water-mixing ratios in the form of rain, graupel, and snow be less than 0.01 kg/kg. The pixels were spatially down-sampled to ensure that the distance between any two pixels always exceeds 25 km. The mean and standard deviation of the temperature and water-vapor profiles in the MM5 data set are shown in Figure 5 and Figure 6, respectively. The histogram of integrated cloud liquid water (liquid-water path) is shown in Figure 7.

The MM5 profiles are generally warmer and contain more water vapor and cloud liquid water than the NOAA88b profiles and are highly representative of the atmospheres that would be the primary focus of the Precipitation and All-weather Temperature and Humidity (PATH) mission. The NOAA88b profiles characterized by

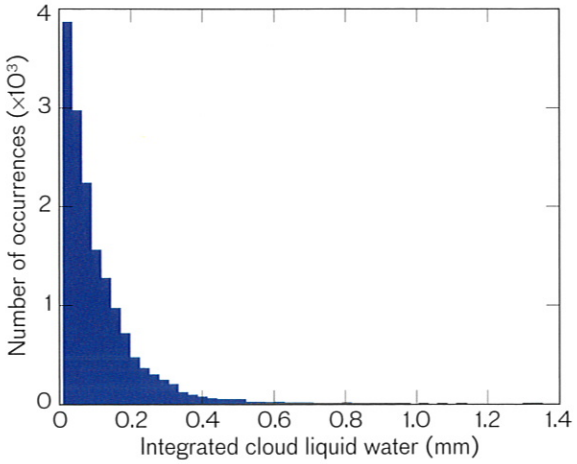

FIGURE 7. The histogram shows the vertically integrated cloud liquid water content (i.e., liquid water path) in the MM5 storm data set. The NOAA88b data set does not include measurements of cloud liquid water. Rain becomes likely when the integrated cloud liquid water content exceeds approximately 0.2 mm. Precipitating pixels have been removed from the data set [16].

a high level of variability are due to the deliberate inclusion of more extreme cases.

Microwave/Millimeter-Wave Non-Scattering Radiative Transfer Model: TBARRAY

Simulated brightness-temperature observations for atmospheric profiles in the NOAA88b data set were calculated using the TBARRAY software package of Rosenkranz [17]. TBARRAY is a line-by-line routine based on the Liebe Millimeter-wave Propagation Model (MPM) [18, 19]. Scattering was not modeled because cloud liquid-water content was not recorded in the NOAA88b data set. All radiative transfer calculations for the temperature and water-vapor retrieval simulations were performed at a single angle at nadir incidence.

Microwave/Millimeter-Wave Scattering Radiative Transfer Model: TBSCAT

Simulated brightness-temperature observations for atmospheric profiles in the MIT MM5 data set were calculated using the TBSCAT software package of Rosenkranz [20]. TBSCAT is a multistream initial-value radiative transfer routine that includes both absorption and scattering. The collection of streams describes a system of coupled first-order differential equations, and TBSCAT approaches the solution as an initial-value problem starting from the top of the atmosphere. The solution uses the backward Euler method of finite differences. The absorption coefficients are calculated identically in TBARRAY and TBSCAT. The scattering calculations comprise the Mie coefficients, the inverse-exponential drop-size distribution (for precipitating cases only), the Liebe/Huord permittivity model, and the Henyey-Greenstein phase function. The scattering coefficients are calculated using the Deirmendjian implementation in the Mie region and the Wiscombe implementation in the Rayleigh region. The clouds in the nonprecipitating MM5 data set were simulated using ten streams and with both the cloud liquid water and cloud ice as scattering hydrometeors. The cloud liquid water was given a radius of 0.02 mm and the cloud ice was given a radius of 0.06 mm, as these values are consistent with recommendations from other investigators [21].

Ocean Surface Emissivity Model: FASTEM and FASTEM2

English and Hewison developed the FASTEM model, which parameterizes an "effective" ocean surface emissivity for frequencies between 10 and 220 GHz for earth incidence angles less than 60° and for oceanic surface wind speeds less than 20 m/s. FASTEM2, an updated version of FASTEM, uses an approach similar to that of Petty and Katsaros to compute the surface emissivity [22, 23]. FASTEM and FASTEM2 both incorporate geometric optics, Bragg scattering, and foam effects. FASTEM was used for the simulations of the precipitating cases, and FASTEM2 (with the optical depth option set to zero) was used for the simulations of the non-precipitating cases. FASTEM and FASTEM2 calculations used the MM5 oceanic wind speed at an altitude of 10 m, which ranged from 0.14 to 11 m/s. The oceanic surface wind speed is not recorded in the NOAA88b data set, and the FASTEM2 wind speed input for these cases was therefore randomized using a uniform distribution between 0.5 and 10 m/s.

Land Surface Emissivity Model

Land surface emissivity values were assigned randomly using a uniform distribution between 0.8 and 1.0. The same emissivity value was used for all frequencies. Recent work has shown that this simple model is fairly representative of most naturally occurring land emissivities, although improvements are planned in future work [24].

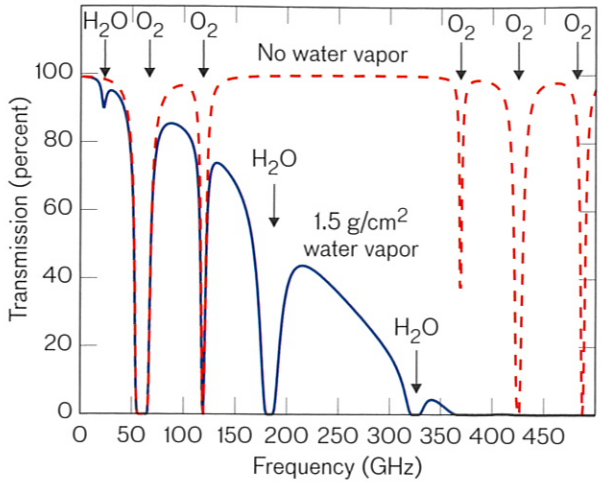

FIGURE 8. There is a clear distinction between water vapor and no water vapor in the microwave/millimeter-wave absorption spectrum. Two calculations for the percent transmission (nadir view) using the 1976 U.S. Standard Atmosphere data are shown, one assuming no water vapor and one assuming 1.5 g/cm^2 (15 mm).

Atmospheric Transmittance at Millimeter Wavelengths: Geostationary Sounding Implications

Atmospheric extinction increases as ~f^4 because of Rayleigh scattering and as ~f^2 because of absorption. Previous work has demonstrated that the relatively high sensitivity of the millimeter-wave bands to hydrometeor scattering can be used to improve precipitation sensing [25–27]. However, the relatively high levels of atmospheric absorption present in millimeter-wave bands can hinder atmospheric sounding in the boundary layer near the surface—a handicap that was explored in the context of geostationary sounding [10].

The microwave/millimeter-wave absorption spectrum is shown in Figure 8 for a fixed amount of water vapor (15 mm) and no cloud liquid water. The characteristic decrease in transmittance with frequency is immediately apparent. The water-vapor content in the 1976 U.S. Standard Atmosphere data used to compute the absorption spectrum shown in Figure 8 is relatively low compared to a typical tropical atmosphere (~50 mm water vapor). Therefore, atmospheric transmittance analysis focuses on profiles from the MIT MM5 data set, which is characterized by high water content. Atmospheric transmittance at nadir incidence at 90 GHz is shown in Figure 9 as a function of the integrated water-vapor content and the integrated cloud liquid-water content, and the transmittance predictably decreases with increasing water content. To explore the frequency and water-content dependence in tandem, the difference between the transmittance at 50 GHz and at 90 GHz as a function of water content is plotted in Figure 10. For low water contents, the transmittance at 90 GHz exceeds that at 50 GHz, although the opposite is true for relatively high water contents. The latter observation is a fundamental limitation of conventional (non-hyperspectral) millimeter-wave sounding. Hyperspectral millimeter-wave systems, however, are able to infer and correct for the increasing atmospheric absorption, even in atmospheres with high water content, because of the very dense vertical spacing of the weighting functions in the atmospheric boundary layer. This important distinction between conventional and hyperspectral sounding will be highlighted later.

Hyperspectral Microwave Physical Retrievals Using Neural Networks

Recent work has demonstrated the utility of atmospheric profile retrievals based on feedforward multilayer perceptron neural networks for both hyperspectral infrared and microwave observations [28, 29]. The execution time of neural network retrievals, once trained using physical models, for example, is typically several orders of magnitude faster than iterated retrievals while offering improved retrieval performance. Neural networks are used in this work to retrieve temperature and moisture profiles and precipitation rates [30].

A neural network is an interconnection of simple computational elements, or nodes, with activation functions that are usually nonlinear, monotonically increasing, and differentiable. Neural networks are able to deduce input-output relationships directly from the training ensemble without requiring underlying assumptions about the distribution of the data. Furthermore, a neural network with only a single hidden layer of a sufficient number of nodes with nonlinear activation functions is capable of approximating any real-valued continuous scalar function to a given precision over a finite domain [31].

A multilayer feedforward neural network consists of an input layer, an arbitrary number of hidden layers (usually one or two), and an output layer. The hidden layers typically contain sigmoidal activation functions of the form

$$z_j = \tanh(a_j), \text{ where } a_j = \sum_{i=1}^{d} w_{ji} x_i + b_j .$$

The output layer is typically linear. The weights w_{ji} and biases b_j for the jth neuron are chosen to minimize a

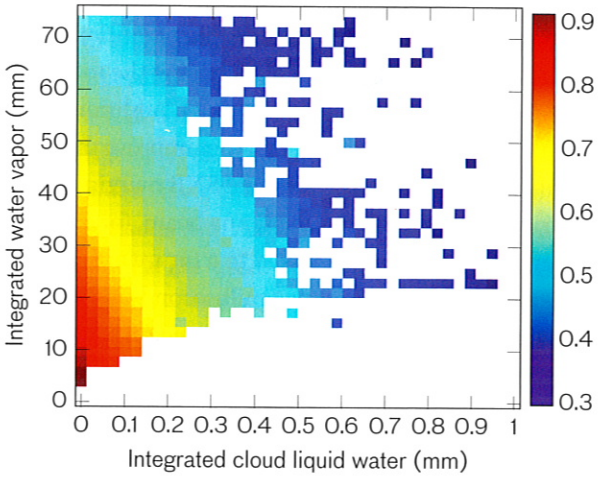

FIGURE 9. These atmospheric transmittance data (at nadir incidence at 90 GHz) were calculated from the MIT MM5 data set. Transmittance values are averaged over bins of integrated water vapor and integrated cloud liquid-water content.

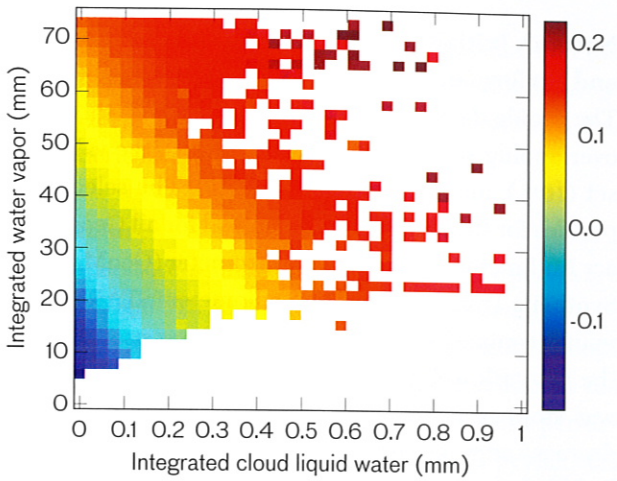

FIGURE 10. Corresponding to Figure 9, these atmospheric transmittance data were calculated from the MIT MM5 data set at nadir incidence at 50 GHz *minus* the MIT MM5 data at 90 GHz.

cost function over a set of P training patterns. A common choice for the cost function is the sum-squared error, defined as

$$E(\mathbf{w}) = \frac{1}{2}\sum_{p}\sum_{k}\left(t_k^{(p)} - y_k^{(p)}\right)^2,$$

where $y_k^{(p)}$ and $t_k^{(p)}$ denote the network outputs and target responses, respectively, of each output node k given a pattern p, and $\mathbf{w}$ is a vector containing all the weights and biases of the network. The training process involves iteratively finding the weights and biases that minimize the cost function through some numerical optimization procedure. Second-order methods are commonly used to carry out the optimization.

Preprocessing with the Projected Principal Components Transform

Hyperspectral sounding systems typically measure atmospheric thermal emission in many spectral bands. The spectral-information content is often correlated, and a linear preprocessing method such as the Projected Principal Components (PPC) transform can be effectively used to reduce the dimensionality and filter noise from the measured spectra, even in the presence of clouds [28, 32]. Furthermore, the PPC transform can be used to optimally extract spectral radiance information that is correlated with a geophysical parameter, such as the temperature or water-vapor profile. The r-rank linear operator that captures the most radiance information correlated to the profile is

$$\mathbf{L}_r = \mathbf{E}_r\mathbf{E}_r^{\mathrm{T}}\mathbf{C}_{TR}(\mathbf{C}_{RR} + \mathbf{C}_{\psi\psi})^{-1},$$

where $\mathbf{E}_r = [\mathbf{E}_1 \mid \mathbf{E}_2 \mid \cdots \mid \mathbf{E}_r]$ are the r most significant eigenvectors of $\mathbf{C}_{TR}(\mathbf{C}_{RR} + \mathbf{C}_{\psi\psi})^{-1}\mathbf{C}_{RT}$, $\mathbf{C}_{RR}$ is the spectral radiance covariance, $\mathbf{C}_{\psi\psi}$ is the noise covariance, and $\mathbf{C}_{TR}$ is the cross-covariance of the atmospheric profile (temperature or water vapor) and the radiance [28]. The hyperspectral millimeter-wave measurements processed in this work were transformed from approximately 100 channels to 25 PPCs for retrieval of both temperature and water-vapor profiles. This factor-of-four reduction in the input dimensionality results in a significant improvement in both the network training time (typically a few hours on a 3 GHz Intel Xeon desktop workstation) and the generalization ability of the neural networks.

Network Topologies

All the temperature and moisture retrievals in this work were implemented using neural networks with a single hidden layer of 15 sigmoidal nodes and a linear output layer with approximately 10 nodes. Approximately five neural networks were aggregated (to achieve approximately 50 total outputs) to estimate the entire profile. Ad hoc attempts were made to optimize the network topology, and this configuration resulted in the best performance. The networks estimate the atmospheric profile up to 20 km for temperature and up to 10 km for water vapor. These estimates and the corresponding *truth* were averaged over 1 km layers prior to the computation of error statistics.

Network Initialization, Training, and Performance Evaluation

The profile data were randomly divided into three nonoverlapping sets: the training set (80%), the validation set (10%), and the testing set (10%). The selection of profiles for the data sets was identical for all Geostationary Millimeter-wave Array Spectrometer (GeoMAS) and Synthetic Thinned Aperture Radiometer (STAR) performance comparisons. The training set was used to derive the network weights and biases. The network training was stopped if the error on the validation set did not decrease after ten consecutive training epochs or if three hundred epochs were reached. Each neural network was trained ten separate times with random initializations, and the validation set was used to select the best of the ten networks. All the neural-network retrieval results were derived using the testing set.

All networks were initialized using the Nguyen-Widrow method [33] and trained using the Levenberg-Marquardt optimization procedure [34, 35]. The NETLAB neural network software package was used to train the networks [36]. Random sensor noise (see the last column of Table 1 and Table 2) was added to each simulated measurement at the beginning of each training epoch.

Notional Systems Used for Comparisons

The performance of the hyperspectral millimeter-wave concept in the geostationary context can be assessed by using two notional systems, an 88-channel system operating near 118 and 183 GHz and a 10-channel system operating near 60 and 183 GHz. The underlying physical and radiometric assumptions for both systems are identical, as discussed below, and identical neural-network retrieval algorithms are used. At this point, there should be no claims of optimality for either of the two notional systems.

Geostationary Millimeter-Wave Array Spectrometer: GeoMAS

The nominal GeoMAS sensor configuration comprises a modest 88-channel hyperspectral millimeter-wave spectrometer—72 channels near the 118.75 GHz oxygen absorption line and 16 channels near the 183.31 GHz water vapor absorption line. This configuration could easily be realized using five dual-polarized antenna horns (sharing a common reflector) each feeding a simple 9-channel receiver bank. The spatial resolution of the water-vapor channels could be doubled by arranging additional feeds in a 2×2-array configuration, thus raising the total number of feedhorns to eight (see Figure 1). Additional feeds and channels could be added to further improve the spatial resolution of both bands (additional SNR margin could be used to sharpen the effective antenna beam, for example), although this analysis is deferred to a future article.

An integration time of 22.5 milliseconds is selected to allow temperature profiles to be retrieved on a 200×200 grid spaced at 50 km (10,000 × 10,000 km coverage area) in 15 minutes. The water-vapor profiles would be retrieved on a 400×400 grid spaced at 25 km (10,000 × 10,000 km coverage area) in 15 minutes.

The GeoMAS channel properties for a single receiver bank (of eight) of the 118 GHz temperature band are summarized in Table 1. System temperatures of 650 and 800 K were assumed for the 118 GHz and 183 GHz systems, respectively. The eight 118 GHz temperature bands (nine channels each) are offset from one another in frequency by 70 MHz, and the band edge of the most opaque channel is approximately 250 MHz from the O_2 line center. A transparent channel at 89 GHz was added to each 118 GHz receiver bank to improve profiling performance at the surface and near the boundary layer. The two 183 GHz water-vapor banks (eight channels each) are offset from one another in frequency by 500 MHz, and the band edge of the most opaque channel is 10 MHz from the H_2O line center. The root-mean-square (RMS) temperature, ΔT_{RMS}, of each water vapor channel is 0.17 K. The frequency offset and overlap values were obtained using simple trial-and-error experiments. Further channel optimizations should improve GeoMAS retrieval performance but are beyond the scope of this article.

Synthetic Thinned-Aperture Radiometer: STAR

A synthetic thinned-aperture radiometer has recently been suggested for geostationary implementation with approximately 900 receivers; 300 operating near 60 GHz and 600 operating near 183 GHz [37, 38]. Using the identical fundamental assumptions as the GeoMAS system—40,000 temperature profiles (50 km grid spacing) and 160,000 water-vapor profiles (25 km grid spacing) derived in 15 minutes—synthetic and unsharpened filled-aperture systems yield comparable image noise levels for comparable receivers and total integration times, provided that both systems survey the entire vis-

ible Earth and have the same bandwidths and receiver-noise temperatures [39].

The STAR configuration follows closely from the work of Lambrigtsen et al., although broader bandwidths have been included (favorable to STAR performance) to facilitate comparisons with AMSU-A/B performance [38]. Ten STAR channels are used: six identical to AMSU-A temperature bands near 60 GHz, three identical to AMSU-B water-vapor bands near 183 GHz, and a single band at 167 GHz. System temperatures are assumed to be 500 K for each 60 GHz receiver and 800 K for each 167/183 GHz receiver. Because each receiver can sample only a single channel at a time, the integration time available to a given channel is equal to the total integration time per pixel (22.5 msec for 60 GHz, 5.625 msec for 183 GHz) divided by the number of channels in the receiver (six near 60 GHz and four near 183 GHz). The STAR channel properties are summarized in Table 2.

Temperature and Moisture Sounding Performance Comparisons

An examination of temperature and water-vapor profile retrieval performances in nonprecipitating atmospheres for both the GeoMAS and STAR notional systems give insights on the benefits of each system. Here, both ocean and land cases are included in equal proportion, and the NOAA88b and MM5 profile sets are analyzed separately. The performance is indicated by RMS errors in 1 km atmospheric layers.

Temperature

The temperature-profile retrieval-performance curves are shown in Figure 11. Also shown is the surface temperature RMS error. The GeoMAS performance is excellent both for the NOAA88b profile set (high variability) and for the MM5 profile set (high water content). GeoMAS performance exceeds STAR performance for both profile sets at all atmospheric levels, including the surface. The performance difference in the relatively moist MM5 profile set is substantial, with approximately a 0.5 K difference in RMS error throughout the troposphere, including the critical atmospheric boundary layer. GeoMAS surface-temperature retrievals are substantially superior to those of STAR, with a difference in RMS error of approximately 1 K. Note that the STAR performance closely resembles that of AMSU-A/B, as the primary tropospheric sounding channels are identical. The absence of relatively transpar-

CHANNEL	OFFSET (GHz)	BANDWIDTH (GHz)	TRMS (K)
1	−4720	560	0.19
2	−4160	560	0.19
3	−3600	560	0.19
4	−3040	560	0.19
5	−2480	560	0.19
6	−1920	560	0.19
7	−1360	560	0.19
8	−800	560	0.19
9	−29,750	1000	0.14

TABLE 1. The GeoMAS channels for a single receiver bank of eight are offset from the 118.75 GHz temperature band. The last column is the RMS of the random sensor noise ΔT_{RMS}.

CHANNEL	CENTER FREQUENCY (GHz)	BANDWIDTH (GHz)	TRMS (K)
1	50.3	180	0.5
2	52.8	400	0.35
3	53.596	170	0.5
4	54.4	500	0.35
5	54.94	400	0.35
6	55.5	350	0.35
7	167	1000	0.71
8	183.31±1	500	1.0
9	183.31±3	1000	0.71
10	183.31±7	2000	0.5

TABLE 2. The individual STAR channel sensitivities are poorer than those for comparable GeoMAS channels because the STAR system must sample each channel separately, thus decreasing the available integration time.

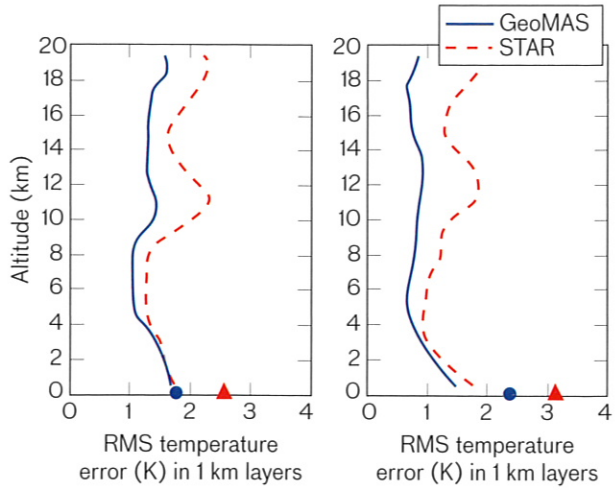

FIGURE 11. A comparison of GeoMAS (118/183 GHz) and STAR (60/183 GHz) temperature-retrieval performance over land and ocean at nadir incidence shows that GeoMAS has lower RMS errors at all altitudes. The left panel shows RMS error in 1 km layers using the NOAA88b data set, and the right panel shows RMS error using the MIT MM5 data set. Surface temperature RMS error is indicated by a circle (GeoMAS) and a triangle (STAR).

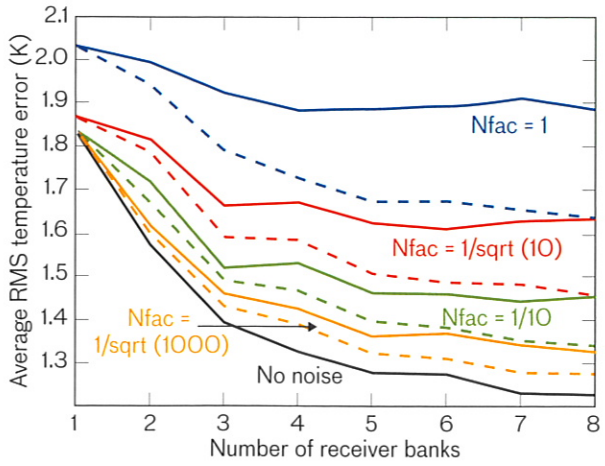

FIGURE 12. Incremental benefits are achieved with each additional eight-channel receiver banks. All curves indicate the RMS temperature-profile error averaged over all atmospheric layers from 0 to 20 km as a function of the number of receiver banks used. The solid curves were calculated by using a fixed bandwidth that is shared among all receiver banks, and the dashed curves are calculated by using a fixed bandwidth for each receiver bank. Each pair of dashed and solid curves was calculated by using a different noise factor (Nfac), which is a simple scaling of the integration time. The dashed and solid curves labeled "no noise" are identical.

ent channels at 23.8 and 31.4 GHz slightly degrades performance in the lower boundary layer, with the primary impact on water-vapor retrieval over ocean.

The GeoMAS performance advantage as indicated in Figure 11 is due to two factors. First, the high density of weighting functions in the vertical dimension, as shown in Figure 3, enables GeoMAS measurements to capture profile information with high vertical resolution. Second, the large total bandwidth afforded by the GeoMAS system allows relatively high sensitivity to be achieved. The bandwidth benefit and the channelization benefit are now explored separately.

Figure 12 shows the RMS temperature profile averaged over all atmospheric layers from 0 to 20 km as a function of the number of receiver banks included in a hyperspectral microwave system. It is obvious that increased sensitivity caused by increased bandwidth will always improve retrieval results, but two more interesting cases now arise. First, a fixed amount of bandwidth is shared among all the receiver banks (the solid curves in Figure 12). Improvement in this case as receiver banks are added is due only to the advantage afforded by increased channelization, resulting in a more dense vertical spacing of the weighting functions. The curves are shown for five different integration times, based on a scaling of the integration time used to generate Figure 11. The top curve corresponds to the same integration time used to generate Figure 11, and this integration time was increased by factors of 10, 100, 1000, and infinity (no noise) to generate the other curves. The second case (the dashed curves in Figure 12) assumes that a fixed amount of bandwidth is allocated for each receiver bank. Both increased bandwidth and increased channelization positively impact performance in this case as receiver banks are added.

These results are characterized by two interesting features. First, the marginal benefit of increased channelization is apparent in all cases. Second, the amount of channelization benefit is more pronounced as the integration time is increased. The temperature-profile retrieval performance is analyzed by assessing the accuracy in the lower boundary layer (the 1 km layer nearest the surface) as a function of the atmospheric transmittance, shown in Figure 13. The errors shown have been normalized by the *a priori* standard deviation of the temperature over all the profiles included in each of 20 transmittance bins. That is, a value of 0.5 indicates that the RMS error is one-half the RMS error that would have resulted by using the mean temperature value (over the bin) as the estimate. The bell-

shaped curve can be explained as follows. Relatively small errors toward the right of the figure result because the high atmospheric transmittance allows the surface temperature to be sensed with high accuracy, and the surface temperature tends to be correlated with the temperature in the lower boundary layer. As transmittance decreases, the surface is increasingly obscured and the error therefore increases. As transmittance decreases beyond 0.6 or so, the contribution from the lower boundary layer to the overall measured radiance for most channels is maximized, and the error therefore decreases. As transmittance approaches zero, the radiative contribution from the lowest 1 km layer decreases because of obscuration by opaque layers above.

Water Vapor

The water-vapor profile retrieval-performance curves are shown in Figure 14. The errors shown are the RMS profile retrieval error divided by the *a priori* standard deviation in the profile set. The GeoMAS performance is excellent both for the NOAA88b profile set (high variability) and for the MM5 profile set (high water content). GeoMAS performance exceeds STAR performance for both profile sets at all atmospheric levels.

Investigation of Additional Error Sources

The simulation analyses presented thus far have been performed under ideal circumstances to accentuate the relative merits of the various sensor systems. Some of the following error sources would be expected under realistic conditions. For example, simulation analyses often assume perfect sensor and atmospheric physics, as well as perfect ground truth, and these assumptions are invalid in practice. Of particular concern are correlated errors that could be especially detrimental to a hyperspectral microwave system comprising many channels with broad, overlapping weighting functions. None of the error sources considered here were presented to the neural-network retrievals during training.

Two-Dimensional Simulation Methodology

Unknown array-misalignment error and spatial-inhomogeneity error are two such correlated error sources. Array misalignment could result from mechanical and/or electrical imperfections in the antenna arrays used to produce the footprints shown in Figure 1. Subpixel spatial inhomogeneities introduced by atmospheric and surface features further degrade performance. Both of these errors were assessed by using the high-resolution gridded MM5 profile set.

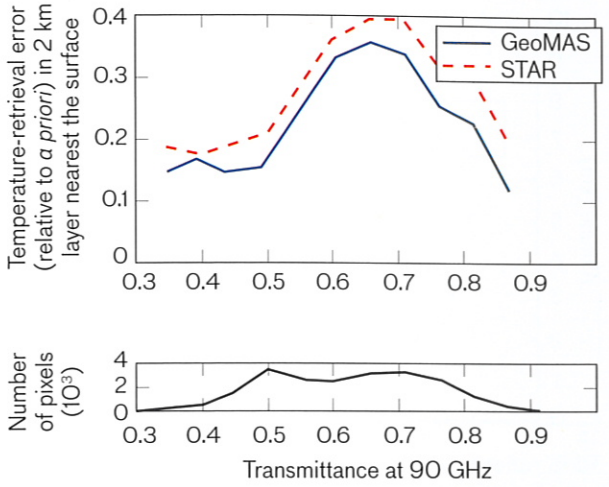

FIGURE 13. A comparison of GeoMAS (118/183 GHz) and STAR (60/183 GHz) temperature-retrieval performance again shows the improvement of GeoMAS over STAR in the 1 km atmospheric layer nearest the surface as a function of transmittance at 90 GHz. The errors are shown relative to the *a priori* standard deviation in the profile set.

Static, unknown misalignment errors of approximately 10% of each temperature sounding footprint and 20% of each water vapor sounding footprint were introduced to the GeoMAS arrays during simulation of the brightness temperatures. This level of unknown misalignment error is expected to be much larger than would be encountered on an actual system. The STAR alignment was assumed to be perfect.

Clouds, surface features, and water vapor are highly variable in the horizontal dimension, and subpixel inhomogeneities across 50 km temperature and 25 km water-vapor footprints are likely. Gaussian antenna-beam patterns for the GeoMAS and STAR systems were convolved with the high-resolution (5 km) brightness-temperature fields calculated using the MM5 profile set to simulate the effects of spatial inhomogeneities.

Simulation Error

An uncorrelated Gaussian random error term with 0.2 K standard deviation and zero mean was added to all calculated brightness temperatures. This added error accounts to first order for imperfections in the surface, transmittance, and radiative transfer models used to derive the retrievals, as well as any errors in the ground truth.

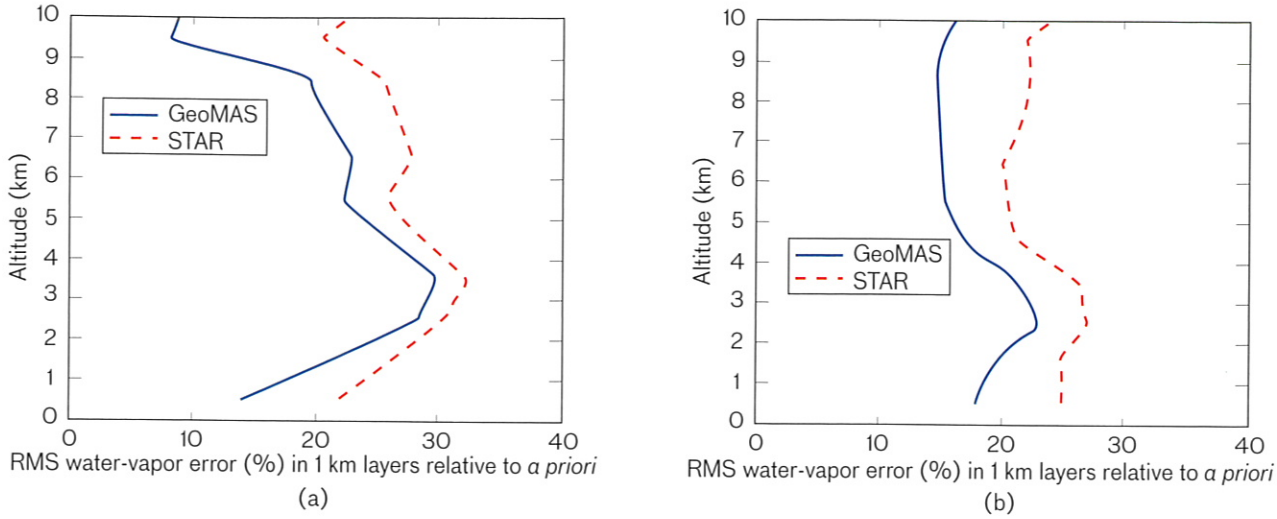

FIGURE 14. GeoMAS (118/183 GHz) water-vapor retrieval performance over land and ocean at nadir incidence data are better than the corresponding STAR (60/183 GHz) performance: (a) the RMS error data (relative to the *a priori* variation in the validation set) in 1 km layers use the NOAA88b data set; (b) the MM5 storm data set is used.

Simulation results

Temperature and water-vapor retrieval results after inclusion of all the error sources above are shown in Figures 15(a) and 15(b), respectively. GeoMAS temperature-profile retrieval RMS performance exceeds 1.5 K in 1 km layers, surface-temperature RMS performance exceeds 2 K, and water-vapor-profile retrieval performance exceeds 30% in 1 km layers. While performance does degrade relative to Figure 11 and Figure 14, it is encouraging to note the high degree of robustness of the GeoMAS system to these error sources. Other sources of error are currently under study (for example, intermediate-frequency filterbank stability) and associated analysis results will be reported in a future publication.

Precipitation Performance Comparison for Notional Geostationary Systems

Airborne and spaceborne retrievals of precipitation from passive opaque millimeter-wave measurements have demonstrated the potential of a geostationary millimeter-wave sensor for precipitation mapping and tracking [27, 40–44]. The rain-rate retrieval performance of the GeoMAS system is now compared to the STAR systems.

Brightness-temperature simulations were carried out using TBSCAT and incorporated a fluffy-sphere ice-scattering model with a wavelength-dependent density $F(\lambda)$ that was tuned to match total scattering cross sections computed for spherical, hexagonal plate, and rosette hydrometeors by using a discrete-dipole electromagnetic scattering model, DDSCAT [14]. Precipitation-retrieval accuracies for GeoMAS and STAR were computed by using neural networks trained using 122 MM5 storms. The algorithms are the same as described by Staelin and Surussavadee, employing three neural networks [39]. If the rain-rate estimates from the first network were over 8 mm/h, then the second neural network was used to estimate the 15-minute average precipitation rate; otherwise, the third network was used. Inputs used to train all three networks include the MM5 precipitation rates blurred to 25 km, a land/sea flag, and the current channel brightness temperatures and those observed 15 minutes earlier. The three layers of each network had ten, five, and one neurons, respectively, for which the first two layers used a hyperbolic tangent sigmoid function. The best of 100 tested networks was used for each network and task, where "best" means the minimum RMS retrieval errors over the full dynamic range. The results, shown in Table 3, indicate excellent performance of GeoMAS relative to STAR in light to moderately heavy rain.

Low Earth-Orbit Systems Performance Simulation Comparisons

The results of sounding performance for low Earth-orbit systems are now examined. Retrieval simulations were performed using the channel sets of the AIRS/AMSU-

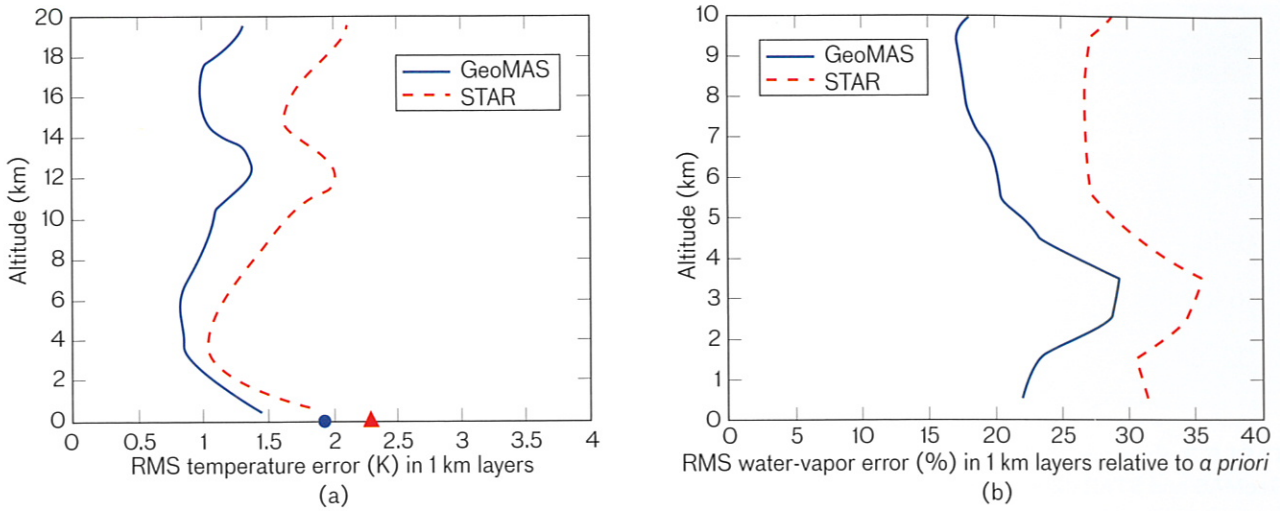

FIGURE 15. This comparison of GeoMAS (118/183 GHz) and STAR (60/183 GHz) two-dimensional temperature-retrieval performance (a) and water vapor performance (b) over land and ocean at nadir incidence uses the MIT MM5 data set with detailed modeling of correlated error sources. In (a), the surface-temperature RMS error is indicated by a circle (GeoMAS) and a triangle (STAR).

A/HSB (for Humidity Sounder for Brazil) sounding suite currently flying on the NASA Aqua satellites and for two notional hyperspectral microwave systems [4]. The notional Hyperspectral Microwave Array Spectrometer (HyMAS) systems include channels near 60 GHz (HyMAS60) and near 118 GHz (HyMAS118). Both HyMAS systems include 16 water-vapor channels near 183 GHz. The HyMAS118 system has identical channels to the GeoMAS system, shown in Table 1. The HyMAS60 system contains 64 channels near oxygen lines in the 60 GHz region, shown in Table 4. Each receiver bank has offset in frequency by 240 MHz. No attempts were made to optimize the channelization of either of the HyMAS systems. As with the GeoMAS simulations, system temperatures at 60 GHz, 118 GHz, and 183 GHz were assumed to be 500 K, 650 K, and 800 K, respectively. An integration time of 165 msec is assumed to closely approximate that of the AMSU-A sensor. (The AMSU-A1 integration time is approximately 165 msec and the AMSU-A2 integration time is approximately 160 msec.) Channel properties of the AIRS (2378 channels), AMSU-A (15 channels), and HSB (4 channels) sensors were obtained from the Aqua level 1B, version 5 channel list files. The AMSU-A/HSB ΔT_{RMS} values have been improved to reflect the system temperatures mentioned above. Actual AMSU/HSB ΔT_{RMS} values are about twice those assumed here, where the recent improvements reported in Kangaslahti et al., have been incorporated [9].

The methods and assumptions used to carry out the retrieval-performance simulations presented here are very similar to those used earlier in this article. Notable differences include the profile database and the simulation and retrieval methodology used for the combined microwave and infrared observations.

The AIRS/AMSU-A/HSB Level 2 Profile Database

Global atmospheric-profile data derived from AIRS/AMSU-A/HSB observations dating back to 30 August 2002 are available from the NASA Data and Information Services Center [45]. The "Version 5 Support Product" (AIRX2SUP) used as the ground truth in the performance-simulation analyses includes temperature, moisture, and cloud liquid-water profiles reported on 100 atmospheric levels with a 45 km horizontal spatial resolution at nadir. This product also includes the retrieved cloud-top pressures and cloud fractions for two cloud layers at each of the nine AIRS fields of view that comprise the AIRS/AMSU-A/HSB field of regard. The AIRS level 2, version 5 quality flag "P_{good}" was required to equal the surface pressure for the profile to be included in the data set. The resulting distribution of cloud fractions in the data set was approximately uniform from 0 to 90%, with a spike near zero with a relative frequency of approximately 10%.

AIRS level 2 profiles and cloud products uniformly distributed from December 2004 to January 2006 were

RAIN-RATE RANGE (mm/h)	GeoMAS (mm/h)	STAR (mm/h)
1–4	1.5	1.5
4–8	3.4	3.7
8–16	6.0	6.8
16–32	10.2	10.6
32–64	16.9	17.9

TABLE 3. Rain-rate retrieval-performance comparison of GeoMAS and STAR data clearly shows that GeoMAS performs equal to or better than STAR at all rain-rate levels. All the terms are RMS errors in millimeters per hour. The data were taken at 25 km spatial resolution.

used to simulate a global training database of cloudy AIRS/AMSU-A/HSB observations over ocean at nadir incidence. A separate validation database was constructed using profiles from seven AIRS focus days from 6 September 2002 to 5 December 2003. A 3×3 "golfball" with nine AIRS/HSB footprints and one AMSU-A footprint was simulated for each of the 80,000 profiles in the simulation training and validation data set (40,000 profiles were included in each set). The Stand-Alone Rapid Transmittance Algorithm (SARTA) was used to simulate the AIRS observations and the TBARRAY algorithm was used to simulate the AMSU-A, HSB, and HyMAS observations [17, 46]. This data set was also used to simulate an ensemble of 45 km HyMAS60 and HyMAS118 footprints. The retrieval methodology used for the HyMAS observations is identical to that presented earlier in the article for GeoMAS.

AIRS/AMSU-A/HSB Cloud Clearing and Retrieval Methodology

The cloudy AIRS observations were first "cloud cleared" by using the microwave observations together with the AIRS 3×3 field of regard to estimate the radiances that would have been observed by AIRS if the scene were cloud-free. The stochastic cloud-clearing (SCC) algorithm was used in this work [47]. The SCC algorithm also produces a degree-of-cloudiness estimate that was used to identify "mostly clear" scenes (approximately the clearest 30%) and "mostly cloudy" scenes (approximately the cloudiest 20%). The microwave and cloud-cleared infrared radiances were then used as inputs to the Projected Principal Components/Neural Network (PPC/NN) algorithm, and the temperature and moisture profiles were estimated [28]. This methodology has been extensively validated with actual AIRS/AMSU observations by using a variety of performance metrics [32, 48].

Simulated Performance Comparisons of HyMAS Systems with AIRS/AMSU-A/HSB

The temperature and water-vapor retrieval performance of the HyMAS60, HyMAS118, AIRS/AMSU-A/HSB, and AMSU-A/HSB-only systems are shown in Figures 16(a) and 16(b), respectively. The same set of 40,000 profiles (from the seven-day 2002–2003 validation set) was used to derive the performance of each of the four systems. It is interesting to note that the performance of HyMAS60 in the mid and lower troposphere is very similar to the performance of the AIRS/AMSU-A/HSB system. HyMAS118 water-vapor sounding performance is also very competitive with AIRS/AMSU-A/HSB. HyMAS improvements could be obtained by optimizing the channel sets (center frequencies and bandwidths) and/or by increasing the total number of temperature-sounding receiver banks.

CHANNEL	CENTER (GHz)	BANDWIDTH (GHz)	TRMS (K)
1	48.1	2220	0.03
2	50.0	1570	0.03
3	51.4	1140	0.04
4	52.3	840	0.04
5	53.0	620	0.05
6	53.6	470	0.06
7	54.0	360	0.06
8	54.4	280	0.07
9	89.0	1000	0.05

TABLE 4. The $HyMAS_{60}$ center frequencies, channel bandwidths, and ΔT_{RMS} are distinct from the GeoMAS and $HyMAS_{118}$ channels shown in Table 1.

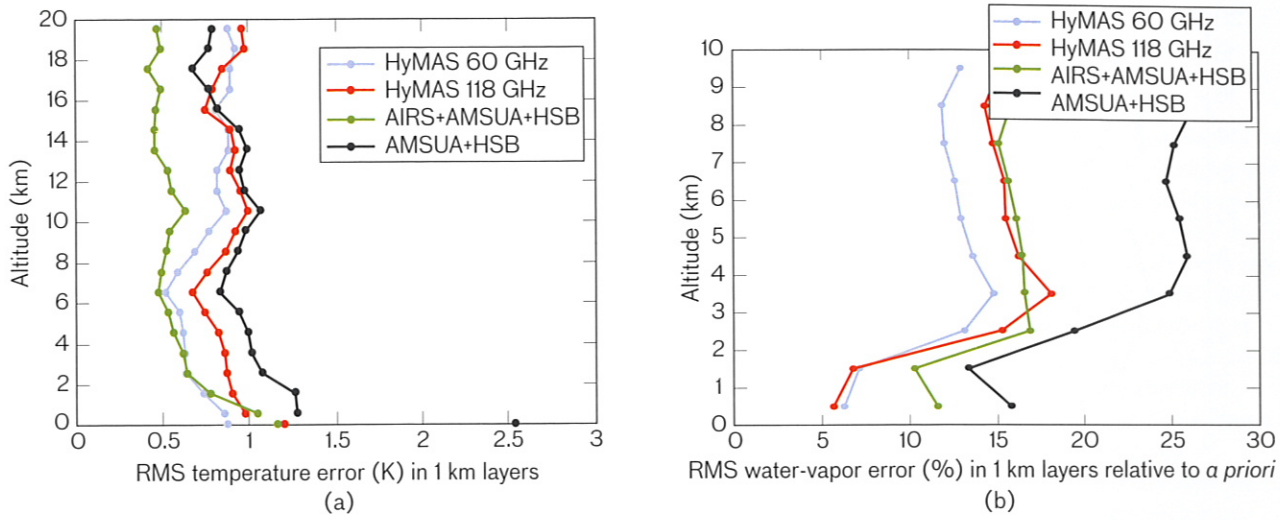

FIGURE 16. Data from seven focus days from 2002 to 2003 were chosen to compare the results of HyMAS60 (60/183 GHz), HyMAS118 (118/183 GHz), AIRS/AMSU-A/HSB, and AMSU-A/HSB-only temperature-retrieval performances (a) and water-vapor retrieval performances (b) over ocean at nadir incidence. For the temperature-retrieval data shown in (a), AMSU-A/HSB noise has been reduced from on-orbit values for consistency with the T_{sys} values used elsewhere.

Simulated Performance Comparisons in Mostly Clear and Mostly Cloudy Conditions

The analysis of simulation performance in mostly clear scenes (favorable to infrared sounding) and in mostly cloudy scenes (favorable to microwave sounding) provides insight into the effectiveness of the HyMAS60 and AIRS/AMSU-A/HSB systems. The temperature and water-vapor retrieval performance of the two systems is shown in Figures 17(a) and 17(b), respectively. The same set of mostly clear or mostly cloudy profiles (from the seven-day 2002–2003 validation set) was used to derive the performance of each system. The mid-tropospheric temperature-sounding performance of AIRS/AMSU-A/HSB is slightly superior to HyMAS60 in mostly clear scenes. HyMAS60 shows a slight advantage in boundary layer temperature retrieval in mostly clear and mostly cloudy conditions and a pronounced advantage (0.6 K difference in RMS) for surface-temperature retrieval in mostly cloudy conditions. HyMAS60 water-vapor sounding performance exceeds AIRS/AMSU-A/HSB for both mostly clear and mostly cloudy scenes.

Future Directions

Hyperspectral microwave-sounding and precipitation-mapping performance could be further improved by spatial processing of Nyquist-sampled observations to sharpen the effective antenna beam. This sharpening amplifies sensor noise, but this increased noise could be offset by adding receiver banks. A promising area of current study is the investigation of the trade-off between effective spatial resolution, receiver array complexity, and retrieval performance. The antenna reflector diameter required to meet a 50 km/25 km temperature/water-vapor resolution goal from geostationary orbit is approximately 2.5 m for a filled-aperture system. However, the results presented in this article together with other work on antenna beam sharpening [39] indicate that such requirements could be met with a GeoMAS system with an antenna reflector diameter smaller than 2 m if image sharpening is used during ground processing. Furthermore, the resolution-versus-noise trade-off can be dynamically optimized, meaning that the level of sharpening can be selected "on the fly" on the basis of the atmospheric scene being viewed. Scenes with high-spatial-frequency content could be detected and sharpening could be used. The selection of the degree of sharpening could be made during ground processing and could be tailored by each user.

While the results presented in this article are encouraging and indicate great promise for future hyperspectral microwave sounding systems, additional analyses and concept demonstration are clearly necessary to study the advantages and challenges of this new sensing modality. Further studies of the error sensitivities of hyperspectral microwave systems are recommended, for example, and

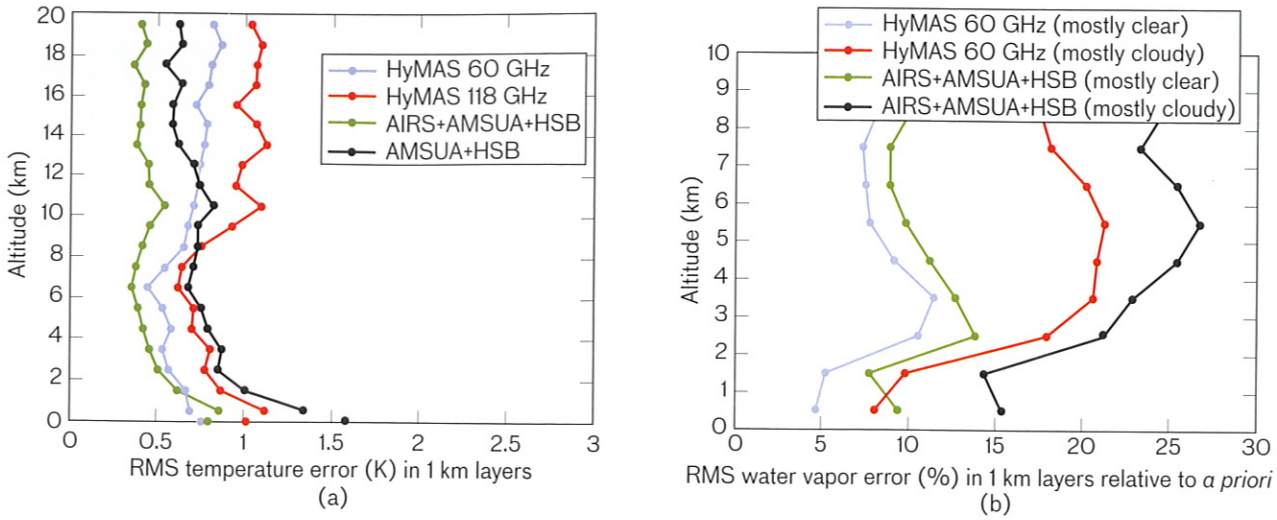

FIGURE 17. Data from seven focus days from 2002 to 2003 were chosen to compare the results of HyMAS60 (60/183 GHz) and AIRS/AMSU-A/HSB temperature-retrieval performances (a) and water-vapor retrieval performances (b) over ocean at nadir incidence in mostly clear and mostly cloudy conditions.

deployment of airborne prototype hyperspectral microwave sensors would provide insight into many of the noise and meteorological phenomena that are difficult to accurately model and simulate.

Another interesting area of further research is the potential synergy resulting from the combined use of hyperspectral microwave and hyperspectral infrared systems. For example, a temperature-profile retrieval of high accuracy provided by a hyperspectral microwave system could be used to substantially improve the estimates of atmospheric carbon dioxide by using an infrared sounder, as the relationship between temperature and carbon dioxide could be decoupled using microwave and infrared measurements.

Acknowledgments

The authors are especially thankful for the thoughtful guidance provided by David Staelin on all facets of this work. The authors gratefully acknowledge helpful discussions with Mike Shields, John Solman, Tim Hancock, Tony Hotz, David Weitz, Greg Berthiaume, Hsiao-hua Burke, and Phil Rosenkranz. This work was funded by the MIT Lincoln Laboratory Advanced Concepts Committee. ■

REFERENCES

1. D.H. Staelin, A.H. Barrett, J.W. Waters, F.T. Barath, E.J. Johnston, P.W. Rosenkranz, N.E. Gaut, and W.B. Lenoir, "Microwave spectrometer on the Nimbus 5 satellite: Meteorological and geophysical data," *Science*, vol. 182, no. 4119, 1973, pp. 1339–1341.
2. W.L. Smith, "Satellite techniques for observing the temperature structure of the atmosphere," *Bull. Am. Meteorol. Soc.*, vol. 53, no. 11, 1972, pp. 1074–1082.
3. W.L. Smith "Atmospheric soundings from satellites—false expectation or the key to improved weather prediction?" *Quarterly J. Royal Meteorol. Soc.*, vol. 117, no. 498, 1991, pp. 267–297.
4. H.H. Aumann, M.T. Chahine, C. Gautier, M.D. Goldberg, E. Kalnay, L.M. McMillin, H. Revercomb, P.W. Rosenkranz, W.L. Smith, D.H. Staelin, L.L. Strow, and J. Susskind, "AIRS/AMSU/HSB on the Aqua mission: Design, science objectives, data products, and processing systems," *IEEE Trans. Geosci. Remote Sens.*, vol. 41, no. 2, 2003, pp. 253–264.
5. G. Chalon, F. Cayla, and D. Diebel, "IASI: An advanced sounder for operational meteorology," *Proc. 52nd Cong. IAF*, October 2001, pp. 1–5.
6. W.L. Smith Sr., H. Revercomb, G. Bingham, A. Larar, H. Huang, D. Zhou, J. Li, X. Liu, and S. Kireev, "Evolution, current capabilities, and future advances in satellite nadir viewing ultraspectral IR sounding of the lower atmosphere," *Atmos. Chem. Phys.*, vol. 9, 2009, pp. 5563–5574.
7. B. Razavi, "A 60 GHz CMOS receiver front-end," *IEEE J. of Solid-State Circuits*, vol. 41, no. 1, 2006, pp. 17–22.
8. J. Powell, H. Kim, and C. Sodini, "SiGe receiver front ends for millimeter-wave passive imaging," *IEEE Trans. on Microwave Theory and Techniques*, vol. 56, 2008, no. 11, pp. 2416–2425.

9. P. Kangaslahti, D. Pukala, T. Gaier, W. Deal, X. Mei, and R. Lai, "Low noise amplifier for 180 GHz frequency band," *2008 IEEE MTT-S Intl. Microwave Symp. Digest*, June 2008, pp. 451–454.
10. W.J. Blackwell and D.H. Staelin, "Comparative performance analyses of passive microwave systems for tropospheric sounding of temperature and water vapor profiles," *GOES-8 and Beyond, SPIE*, vol. 2812, 1996, pp. 472–478.
11. D. Staelin, J. Kerekes, and F.J. Solman, "Geosynchronous microwave sounder working group (GMSWG): final report," Lexington, Mass.: MIT Lincoln Laboratory, August 22, 1997, prepared for NOAA/NESDIS GOES Program Office.
12. A. Lipton, "Satellite sounding channel optimization in the microwave spectrum," *IEEE Trans. Geosci. Remote Sens.*, vol. 41, no. 4, 2003, pp. 761–781.
13. C. Muth, P. Lee, J. Shiue, and W.A. Webb, "Advanced technology microwave sounder on NPOESS and NPP," *IEEE IGARSS Proc.*, vol. 4, 2004, pp. 2454–2458.
14. C. Surussavadee and D.H. Staelin, "Comparison of AMSU millimeter-wave satellite observations, MM5/TBSCAT predicted radiances, and electromagnetic models for hydrometeors," *IEEE Trans. Geosci. Remote Sens.*, vol. 44, no. 10, 2006, pp. 2667–2678.
15. C. Surussavadee and D.H. Staelin, "Millimeter-wave precipitation retrievals and observed-versus-simulated radiance distributions: Sensitivity to assumptions," *J. Atmos. Sci.*, vol. 64, no. 11, 2007, pp. 3808–3826.
16. F.J. Wentz, "A well-calibrated ocean algorithm for SSM/I," *J. Geophys. Res.*, vol. 102, 1997, pp. 8703–8718.
17. P.W. Rosenkranz, "Absorption of microwaves by atmospheric gases," *Atmospheric Remote Sensing by Microwave Radiometry*, M. A. Janssen, Ed. New York: Wiley, 1993, pp. 37–90.
18. H.J. Liebe, "MPM: An atmospheric millimeter-wave propagation model," *Intl. J. Infrared and Millimeter Waves*, vol. 10, no. 6, 1989, pp. 631–650.
19. H.J. Liebe, P.W. Rosenkranz, and G.A. Huord, "Atmospheric 60 GHz oxygen spectrum: New laboratory measurements and line parameters," *J. Quant. Spectrosc. Radiative Transfer*, vol. 48, no. 5–6, 1992, pp. 629–643.
20. P.W. Rosenkranz, "Radiative transfer solution using initial values in a scattering and absorbing atmosphere with surface reflection," *IEEE Trans. Geosci. Remote Sens.*, vol. 40, no. 8, 2002, pp. 1889–1892.
21. F.T. Ulaby, R.K. Moore, and A.K. Fung, *Microwave Remote Sensing Fundamentals and Radiometry*, Norwood, Mass.: Artech House Inc., 1981.
22. S. English and T. Hewison, "A fast generic millimeter-wave emissivity model," *SPIE Proc.*, vol. 3503, 1998, pp. 288–300.
23. G.W. Petty and K.B. Katsaros, "The response of the SSM/I to the marine environment. Part II: A parameterization of the effect of the sea surface slope distribution on emission and reflection," *J. Atmos. Oceanic Tech.*, vol. 11, 1994, pp. 617–628.
24. F. Karbou, C. Prigent, L. Eymard, and J. R. Pardo, "Microwave land emissivity calculations using AMSU measurements," *IEEE Trans. Geosci. Remote Sens.*, vol. 43, 2005, pp. 948–959.
25. A.J. Gasiewski, "Numerical sensitivity analysis of passive EHF and SMMW channels to tropospheric water vapor, clouds, and precipitation," *IEEE Trans. Geosci. Remote Sens.*, vol. 30, no. 5, 1992, pp. 859–869.
26. C. Prigent, J.R. Pardo, and W.B. Rossow, "Comparisons of the millimeter and submillimeter bands for atmospheric temperature and water vapor soundings for clear and cloudy skies," *J. Appl. Meteorol. Climatology*, vol. 45, 2006, pp. 1622–1633.
27. D.H. Staelin and F.W. Chen, "Precipitation observations near 54 and 183 GHz using the NOAA-15 satellite," *IEEE Trans. Geosci. Remote Sens.*, vol. 38, no. 5, 2000, pp. 2322–2332.
28. W.J. Blackwell, "A neural-network technique for the retrieval of atmospheric temperature and moisture profiles from high spectral resolution sounding data," *IEEE Trans. Geosci. Remote Sens.*, vol. 43, no. 11, 2005, pp. 2535–2546.
29. W.J. Blackwell, "Neural network retrievals of atmospheric temperature and moisture profiles from high-resolution infrared and microwave sounding data," *Signal and Image Processing for Remote Sensing*, C.C. Chen, Ed., Boca Raton, Fla.: Taylor and Francis, 2006, pp. 205–232.
30. W.J. Blackwell and F.W. Chen, *Neural Networks in Atmospheric Remote Sensing*, Boston: Artech House, 2009.
31. K.M. Hornik, M. Stinchcombe, and H. White, "Multilayer feedforward networks are universal approximators," *Neural Networks*, vol. 4, no. 5, 1989, pp. 359–366.
32. W.J. Blackwell, M. Pieper, and L.G. Jairam, "Neural network estimation of atmospheric profiles using AIRS/IASI/AMSU in the presence of clouds," *Proc, SPIE—Intl. Soc. Optical Engineering*, vol. 7149, 2008, pp. 714905–714916.
33. D. Nguyen and B. Widrow, "Improving the learning speed of two-layer neural networks by choosing initial values of the adaptive weights," *Intl. Joint Conf. Neural Networks*, vol. 3, 1990, pp. 21–26.
34. D. Marquardt, "An algorithm for least-squares estimation of nonlinear parameters," *J. Soc. Indus. Appl. Math.*, vol. 11, no. 2, 1963, pp. 431–441.
35. M.T. Hagan and M.B. Menhaj, "Training feedforward networks with the Marquardt algorithm," *IEEE Trans. Neural Networks*, vol. 5, 1994, pp. 989–993.
36. I.T. Nabney, *NETLAB: Algorithms for Pattern Recognition*, London: Springer, 2002.
37. A. Tanner, W. Wilson, B. Lambrigsten, S. Dinardo, S. Brown, P. Kangaslahti, T. Gaier, C. Ruf, S. Gross, B. Lim, S. Musko, S. Rogacki, and J. Piepmeier, "Initial results of the geostationary synthetic thinned array radiometer (GeoSTAR) demonstrator instrument," *IEEE Trans. Geosci. Remote Sens.*, vol. 45, no. 7, 2007, pp. 1947–1957.
38. B. Lambrigtsen, S. Brown, T. Gaier, P. Kangaslahti, and A. Tanner, "A baseline for the decadal-survey path mission," *IGARSS 2008—2008 IEEE Intl. Geosci. Remote. Sensing Symp., Proc. Remote Sensing Active and Passive: Volume I Microwave*, vol. 3, 2008, pp. 338–341.
39. D.H. Staelin and C. Surussavadee, "Precipitation retrieval accuracies for geo-microwave sounders," *IEEE Trans. Geosci. Remote Sens.*, vol. 45, no. 10, 2007, pp. 3150–3159.

40. W.J. Blackwell, J.W. Barrett, F.W. Chen, R.V. Leslie, P.W. Rosenkranz, M.J. Schwartz, and D.H. Staelin, "NPOESS aircraft sounder testbed-microwave (NAST-M): Instrument description and initial flight results," *IEEE Trans. Geosci. Remote Sens.*, vol. 39, no. 11, 2001, pp. 2444–2453.
41. R.V. Leslie and D.H. Staelin, "NPOESS aircraft sounder testbed-microwave: Observations of clouds and precipitation at 54, 118, 183, and 425 GHz," *IEEE Trans. Geosci. Remote Sens.*, vol. 42, no. 10, 2004, pp. 2240–2247.
42. F.W. Chen and D.H. Staelin, "AIRS/AMSU/HSB precipitation estimates," *IEEE Trans. Geosci. Remote Sens.*, vol. 41, no. 2, 2003, pp. 410–417.
43. C. Surussavadee and D.H. Staelin, "Global millimeter-wave precipitation retrievals trained with a cloud-resolving numerical weather prediction model, Part I: Retrieval design," *IEEE Trans. Geosci. Remote Sens.*, vol. 46, no. 1, 2008, pp. 99–108.
44. C. Surussavadee and D.H. Staelin, "Global millimeter-wave precipitation retrievals trained with a cloud-resolving numerical weather prediction model, Part II: Performance evaluation," *IEEE Trans. Geosci. Remote Sens.*, vol. 46, no. 1, 2008, pp. 109–118.
45. NASA Goddard Earth Sciences Data and Information Services Center: http://disc.sci.gsfc.nasa.gov/AIRS/data-holdings
46. L. Strow, S. Hannon, and S. Desouza-Machado, "An overview of the AIRS radiative transfer model," *IEEE Trans. Geosci. Remote Sens.*, vol. 41, no. 2, 2003, pp. 303–313.
47. C. Cho and D.H. Staelin, "AIRS observations versus numerical weather predictions of cloud-cleared radiances," *J. Geophys. Res.*, vol. 111, 2006, D09S19.
48. H.H. Aumann, E. Manning, C. Barnet, E. Maddy, and W. Blackwell, "An anomaly correlation skill score for the evaluation of the performance of hyperspectral infrared sounders," *Atmospheric and Environmental Remote Sensing Data Processing and Utilization V: Readiness for GEOSS III. Proc. SPIE*, vol. 7456, 2009, pp. 74560T-1–74560T-7.

ABOUT THE AUTHORS

William Blackwell is a senior member of the technical staff in the Sensor Technology and System Applications Group. Since 2002, he has worked at MIT Lincoln Laboratory in the area of atmospheric remote sensing, including the development and calibration of airborne and spaceborne microwave and hyperspectral infrared sensors, the retrieval of geophysical products from remote radiance measurements, and the application of electromagnetic, signal processing, and estimation theory. He received a bachelor's degree in electrical engineering from the Georgia Institute of Technology in 1994 and master's and doctorate degrees in electrical engineering and computer science from the Massachusetts Institute of Technology. Bill has received numerous honors and awards, including the 2009 NOAA David Johnson Award for his work in neural-network retrievals and microwave calibration, and holds various roles on technical committees and nationally sponsored projects.

Vincent Leslie is a member of the technical staff in the Sensor Technology and System Applications Group. He received a doctorate degree in electrical engineering from Massachusetts Institute of Technology in 2004, where he was a graduate research assistant for the Remote Sensing and Estimation Group at the Research Laboratory of Electronics, specializing in passive microwave radiometry. He received a bachelor's degree from Boston University in 1998 and a master's degree from MIT in 2000, both in electrical engineering. He is a member of the Order of the Engineer.

Michael Pieper is an associate technical staff member in the Sensor Technology and System Applications Group. He received bachelor's and master's degrees in electrical engineering from Northeastern University. Since 2007, he has been involved with the development of hyperspectral infrared imaging detection and discrimination algorithms for the ARTEMIS sensor on the TacSat-3 satellite and atmospheric-profile-retrieval algorithm development for the AIRS/AMSU sensor suite on the NASA Aqua satellite.

Jenna Samra is an associate staff member in the Sensor Technology and System Applications Group. Her current work includes developing algorithms to process data from satellite-based atmospheric sensing instruments and building a test bed to experimentally verify an image-restoration algorithm for large telescopes. She received bachelor's and master's degrees in electrical engineering from the Pennsylvania State University.